IEEE Photonics Journal
An IEEE Photonics Society Publication

Open Access

Device Characteristics of Top-Emitting Organic Light-Emitting Diodes Depending on Anode Materials for CMOS-Based OLED Microdisplays

Volume 10, Number 6, December 2018

Hyunkoo Lee
Hyunsu Cho
Chun-Won Byun
Chan-Mo Kang
Jun-Han Han
Jeong-Ik Lee
Hokwon Kim
Jeong Hwan Lee
Minseok Kim
Nam Sung Cho

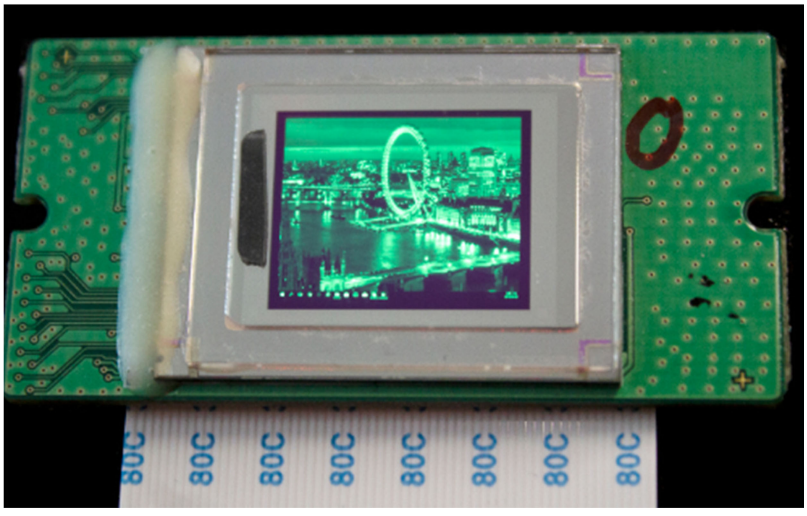

DOI: 10.1109/JPHOT.2018.2877196
1943-0655

IEEE photonics SOCIETY

IEEE

Device Characteristics of Top-Emitting Organic Light-Emitting Diodes Depending on Anode Materials for CMOS-Based OLED Microdisplays

Hyunkoo Lee,[1] **Hyunsu Cho**,[1] **Chun-Won Byun**,[1] **Chan-Mo Kang**,[1] **Jun-Han Han**,[1] **Jeong-Ik Lee**,[1] **Hokwon Kim**,[2] **Jeong Hwan Lee**,[2] **Minseok Kim**,[2] **and Nam Sung Cho**[1]

[1]Flexible Device Research Group, Reality Device Research Division, Electronics and Telecommunications Research Institute (ETRI), Daejeon, 34129, South Korea
[2]RAONTECH, Gyeonggi-do, 13567, South Korea

DOI:10.1109/JPHOT.2018.2877196

Manuscript received September 17, 2018; revised October 17, 2018; accepted October 17, 2018. Date of publication October 22, 2018; date of current version November 5, 2018. This work was supported in part by the National Research Council of Science & Technology (NST) grant by the Korean government (MSIT) (No. CMP-16-05-ETRI, Development of OLED Micro-display Technology for Integrated helmet in Military Application) and in part by In the Institute for Information & Communications Technology Promotion (IITP) grant funded by the Korean government (MSIT) in 2018 (No. 2018-0-01035, Development of Augmented Reality-based Life Safety Content Service Platform for the Low-vision). Corresponding author: Hyunkoo Lee (email: lhk108@etri.re.kr).

Abstract: We investigated the optical reflectance, surface roughness, and sheet resistance of aluminum (Al)/titanium nitride (TiN), titanium (Ti), and tungsten (W) layers on Si substrates, which are available in the CMOS foundry, for organic light-emitting diode (OLED) microdisplays. The devices with different metal anode layers exhibited different hole-injection properties and OLED performances, owing to the different optical and electrical properties of metal anode layers. Based on the OLED characteristics, the Al/TiN layer was selected as an anode layer for OLED microdisplays. A green monochromatic OLED microdisplay panel was designed and implemented using the 0.11-μm CMOS process. The density of pixels was ~2 351 pixels per inch and the panel's active area was 0.7 in in diagonal. The resolution of the panel was 1 280 $\times$ 3 $\times$ 1 024, corresponding to SXGA. The panel was successfully operated, and the maximal luminance was ~460 cd/m^2.

Index Terms: Organic light-emitting diodes (OLEDs), microdisplay, OLEDoS, CMOS.

1. Introduction

Recently, virtual reality (VR) and augmented reality (AR) technologies have attracted significant attention, owing to their potential application in next-generation smart devices [1]–[3]. Most VR and AR devices are head-mounted or eye-glass-type wearable devices [4]–[6]. In these devices, displays are very important for enhancing immersion, because most humans are more receptive to information in the visual modality, compared with other modalities such as auditory, tactile, olfactory, and gustatory. Because VR and AR devices are typically head-mounted, and because the display-eye distance is quite short, the displays of these devices should have high resolution, small weight, small size, and low power consumption [7]. Mobile phones and full-color display panels with thin-film transistors (TFT) based on glass substrates are typically used as displays

in VR applications. However, these panels are heavy and bulky, which is not suitable for mobile devices. In addition, the resolution of display panels with glass substrates is quite low, owing to some limitations of the TFT process, resulting in the eye fatigue [8].

Microdisplays that use complementary metal-oxide-semiconductor (CMOS) circuits can present a solution for VR and AR displays, owing to their high resolution and small size. Liquid crystal on silicon (LCoS) microdisplay panels are widely used for head-mounted displays (HMDs), head-up displays (HUDs), and large-size projectors. However, LCoS need additional sources of light and complex optical systems for HMDs, increasing the panel size and weight. Moreover, a narrow range of operating temperatures and a slow response time of LCs can limit the range of potential applications. Lately, organic light-emitting diodes (OLEDs) on silicon (OLEDoS) microdisplays have been proposed as an alternative solution, because OLEDs are self-emissive displays, which implies that no additional light-sources are required and the optical system is relatively simple. Furthermore, OLEDs exhibit a high contrast ratio, a wide range of operating temperatures, and a fast response time, compared with LCs.

OLEDoSs are fabricated using opaque single crystalline silicon (Si) substrates and CMOS processes, which is different from conventional OLED panels with glass substrates and TFTs. Therefore, OLEDoSs use a top-emitting device structure, and available materials for the bottom electrode are limited. The bottom electrode should be highly reflective in the visible range and should have low surface roughness and high work function for efficient injection of holes. A silver (Ag)/indium tin oxide (ITO) bi-layer structure can be a good bottom electrode for top-emitting OLEDs (TEOLEDs), owing to the high reflectance of Ag and high work function of ITO [9]. However, Ag and ITO are not currently supported by the general CMOS foundry. Tungsten (W), titanium (Ti), and aluminum (Al) are available as bottom anodes of OLEDoSs in the general CMOS foundry. In the case of Al, it has high reflectance, but its work function is low for effective injection of holes; in addition, an oxidation problem exists. Titanium nitride (TiN) has the CMOS compatibility and a proper work function which can be used as an anode in OLEDs, but it has low optical reflectance and high sheet resistance compared with Al [10]. Therefore, Al/TiN bi-layer is more advantageous for OLEDoSs as an anode compared with pure Al or TiN [11].

In this work, we investigated optical reflectance, surface roughness, and sheet resistance of Al/TiN, Ti, and W layers on Si substrates that are available in the CMOS foundry. We also fabricated hole-only devices (HODs) with Al/TiN, Ti, and W anodes, and compared their current density-voltage (*J-V*) characteristics. Because different anode layers have different work functions, they exhibit different *J-V* characteristics, which implies different hole-injection properties. The TEOLEDs with Al/TiN, Ti, and W anodes have different performances, owing to the different optical and electrical properties of anode materials. Based on the analysis results for each anode material, we fabricated green monochromatic OLED microdisplay panels with Al/TiN anodes using the 0.11 μm CMOS process, and successfully operated the fabricated panel. To the best of our knowledge, this is the first SXGA resolution OLED microdisplay panel in South Korea [12].

2. Experimental Details

Al, TiN, and Ti were deposited on Si wafers using a sputter (ENDURA-5500, AMAT), and W was deposited using the chemical vapor deposition (CVD) (P-5000 Wxz, AMAT) method, using the CMOS metal process (National Nanofab Center (NNFC), South Korea), and patterned for HOD and TEOLED fabrication. The active area of HODs and TEOLEDs was 2×2 mm^2. The backplanes of the OLED microdisplay panels were fabricated by a commercial foundry company, and contained CMOS IC for OLED microdisplay driving. The 0.11 μm CMOS process was used for CMOS ICs, and 1.2–5.5 V dual voltage was available. All substrates were fabricated on 8-inch Si wafers, and were diced before the OLED process. 40 backplane substrates were obtained in an 8 inch Si wafer. Diced substrates were sequentially cleaned with acetone and methanol, and were rinsed with deionized water. The cleaned substrates were dried in a vacuum oven at 120 °C. All organic materials and top cathode metals were deposited using the vacuum thermal evaporation method. The fabricated devices were transferred to an inert environment glove-box, where they were encapsulated

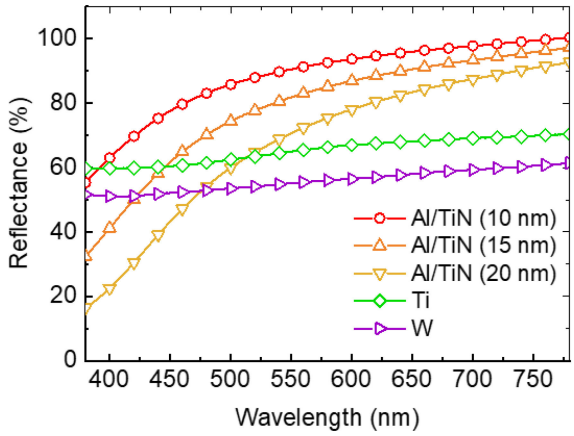

Fig. 1. Optical reflectance of the different anode metal layers of OLEDs, in the visible range.

using an ultraviolet (UV)-curable epoxy and a glass cap containing a moisture getter. Chip on board (COB) bonding process were applied for module packaging. The OLED microdisplay panel had 83 pads and the pads were connected to panel mounting printed circuit board (PCB) by wire bonding. A 60 channel flexible PCB (FPCB) was used for connecting the OLED microdisplay panel and the driving circuit board. Low-voltage differential signaling (LVDS) were used for signal interface.

The optical reflectance values of the different metal layers were measured using an UV-visible-near-infrared (UV-Vis-NIR) spectrophotometer (LAMBDA 750, PerkinElmer). A flat Al mirror (B0071519, PerkinElmer) was used as a reference. An atomic force microscope (AFM) (XE-100, Park Systems) was used for measuring the surface roughness of the metal layers. The sheet resistance values of the metal layers were measured using a four-point probe (CMT-SR2000N, CHANG MIN CO., LTD). Auger electron spectroscopy (AES) (MICROLAB 350, Thermo Electron corporation) and X-ray photoelectron spectroscopy (XPS) (ESCALAB 200R, VG scientific) were used to analyze the relative amounts of atomic elements in the metal layers. The *J-V* characteristics of devices were measured using a source-measure unit (Keithley-238, Keithley), and the luminance (*L*) and electroluminescence (*EL*) spectra were examined using a spectroradiometer (CS-2000, Konica Minolta). All measurements were conducted at room temperature, and the optical reflectance and *J-V-L* were measured in a dark room. Efficiencies were calculated from the luminance, current density, and *EL* spectrum data.

3. Results

We investigated the optical properties of the different anode metal layers because high optical reflectance is required for efficient TEOLEDs. Fig. 1 shows the optical reflectance results for the different anode metal layers of OLEDs, in the visible range. The Al (100 nm)/TiN layer exhibited higher reflectance compared with the Ti (100 nm) and W (100 nm) layers. The optical reflectance of the Al/TiN layer increased with decreasing the TiN thickness. For example, the reflectance values for Al/TiN (10 nm), Al/TiN (15 nm), Al/TiN (20 nm), Ti, and W were 90.5%, 81.8%, 70.7%, 65.0%, and 55.2% at 550 nm, respectively, assuming that the optical reflectance of Al is 100%. Moreover, the Al/TiN layer reflected more light in the red region compared with the blue region, while the other metal layers exhibited a small wavelength-dependent change in reflectance. This result suggests that the Al with the thin TiN layer is optically advantageous for reflective metal anodes of OLEDoSs, compared with the other metal layers, although the Al/TiN layer has high absorption in the blue region.

Surface roughness of anode metal layers of OLEDs is also very important for stable device operation, because common organic layers in OLEDs are very thin, ~100–200 nm. Fig. 2 shows

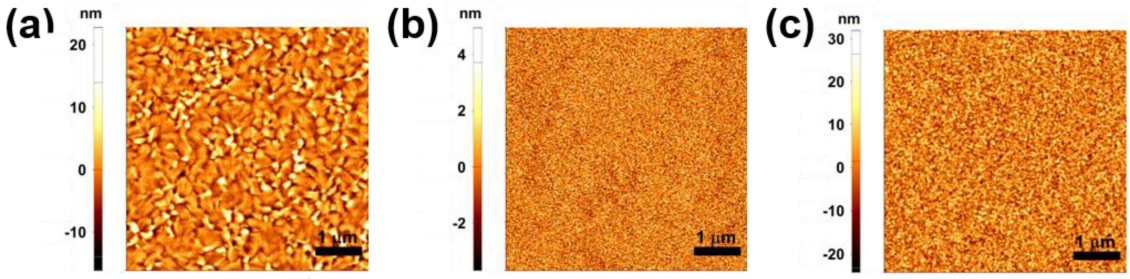

Fig. 2. AFM images ($5 \times 5\ \mu m^2$) of the different metal layers of (a) Al/TiN (10 nm), (b) Ti, and (c) W layers on a Si wafer.

TABLE 1
Properties of the CMOS Process-Based Metal Layers on Si Wafers

Metal layer	Optical reflectance (%)[1] at 550 nm	RMS surface roughness (nm)	Sheet resistance (Ω/□)
Al (100 nm)/TiN (10 nm)	90.5	2.96	0.279
Al (100 nm)/TiN (15 nm)	81.8	2.87	0.274
Al (100 nm)/TiN (20 nm)	70.7	3.02	0.268
Ti (100 nm)	65.0	1.12	5.994
W (100 nm)	55.2	6.87	2.273

[1]Relative value compared with the optical reflectance of the Al.

AFM images of the Al (100 nm)/TiN (10 nm), Ti (100 nm), and W (100 nm) layers. Each metal layer has a different surface morphology. The Al/TiN layer have many grains and grain boundaries due to below Al layer [13]. These grain boundaries may form deep valleys and high peaks, which results in relatively high peak-to-valley roughness of ∼38.93 nm. On the other hand, there is no evident grain and grain boundary in the Ti layer which have relatively low peak-to-valley roughness of ∼8.65 nm [14]. Therefore, the Al/TiN (10 nm) layer exhibits relatively higher root-mean-square (RMS) surface roughness value of ∼2.96 nm compared with that of Ti. In the case of W, the RMS roughness is ∼6.87 nm which is a slightly higher value compared with the other metal layers. Since all anode metal layers have low RMS surface roughness, they can be utilized as bottom electrodes of OLEDs.

We also measured the sheet resistance of metal layers. Al (100 nm)/TiN (10 nm), Ti (100 nm), and W (100 nm) demonstrated sheet resistances of 0.279 Ω/□, 5.994 Ω/□, and 2.273 Ω/□, respectively. All metal layers had low sheet resistances, compared with the sheet resistance of conventional ITO (150 nm), which is ∼10 Ω/□. The properties of the CMOS process-based metal layers are summarized in Table 1.

To investigate the hole-injection property of metal layers, we fabricated HODs with different bottom metal anodes. The HODs had the following structure, as shown in the inset of Fig. 3(a): Al (100 nm)/TiN (10 nm) or Ti (100 nm) or W (100 nm) as bottom metal anodes, /1,4,5,8,9,11-hexaazatriphenylene-hexacarbonitrile (HAT-CN, 10 nm) as a hole-injecting layer, (HIL)/1,1-bis((di-4-olylamino)phenyl)cyclohexane (TAPC, 100 nm) as a hole-transporting layer (HTL)/Al as a top cathode. The HOD with the Al/TiN (10 nm) anode exhibited a slightly higher current density compared with the device with Ti, as shown in Fig. 3(a). The slightly higher work function of TiN compared with Ti may enhance hole injection, as shown in Fig. 3(b) [15], [16]. However, the device

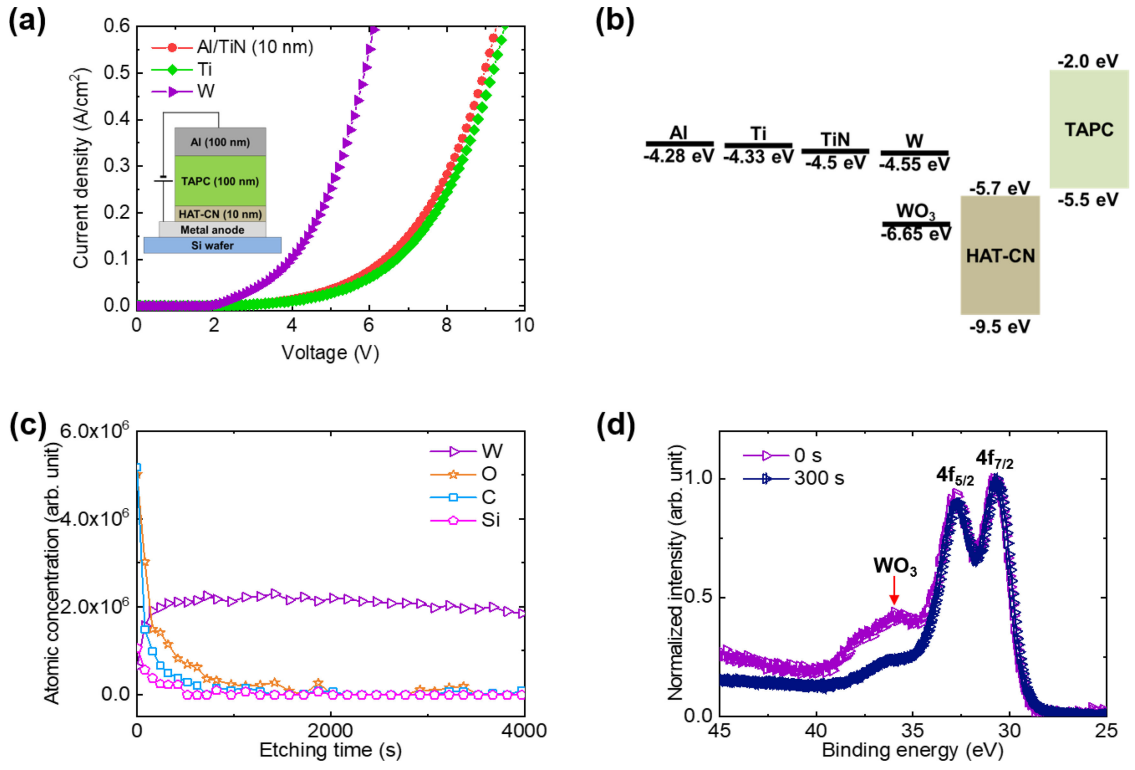

Fig. 3. (a) *J-V* characteristics of HODs (Inset: schematic device structure of the HOD). (b) Energy level diagram of metal and organic layers used in HODs. (c) AES plot. (d) XPS spectra of the W layer on a Si wafer.

with the W anode exhibited a much higher current density compared with devices with other metal anodes, although the work function difference between W and TiN is small. However, WO_3 exhibited a very deep work function energy level [17], as shown in Fig. 3(b). Because deep work function energy level increases the hole injection effectiveness, a WO_3 layer is commonly used as a HIL in OLEDs and quantum-dot LEDs [18], [19]. A W layer on a Si wafer was analyzed using AES and XPS, to inspect whether the surface of the W layer was oxidized or not. Oxygen (O) existed on the surface of the W layer, and the concentration of O decreased with increasing etching time, as shown in Fig. 3(c). Fig. 3(d) shows the XPS spectra of a W layer on a Si wafer, for different etching times. The spectra were normalized to the binding energy of 30.8 eV, which corresponds to the $4f_{7/2}$ peak of W [19]. The spectra exhibited peaks at ~30.8 eV and ~32.8 eV, which corresponded to the $4f_{7/2}$ and $4f_{5/2}$ peaks of W, respectively, regardless of the etching time. However, the peak at 35.8 eV decreased as the etching time increased, and this peak was attributed to WO_3 [20]. This suggests that some parts of the W surface layer on the Si wafer became WO_3 by natural oxidation, resulting in the efficient hole injection.

We fabricated TEOLEDs with the following device structure: Si wafer/(Al (100 nm)/TiN (10 nm)) or (Ti (100 nm)) or (W (100 nm)) as bottom metal anodes, /1,4,5,8,9,11-hexaazatriphenylene-hexacarbonitrile (HAT-CN, 10 nm) as a HIL/N,N'-diphenyl-N,N'-bis(1-naphthyl)-1,1'-biphenyl-4,4"-diamine (NPB, 50 nm) as a HTL/Tris (8-hydroxyquinoline) aluminum (Alq_3, 50 nm) as an emitting layer (EML) and electron-transporting layer (ETL)/ytterbium (Yb, 5 nm) as an electron-injecting layer (EIL)/Ag (25 nm), as a semi-transparent top cathode/NPB (60 nm), as a capping layer. Figs. 4(a) and (b) show, respectively, the *J-V* and *L-V* characteristics of devices with different bottom metal anodes. The device with the W anode exhibited a higher current density compared with the other devices. The devices with Al/TiN (10 nm) and Ti exhibited similar current density values at that

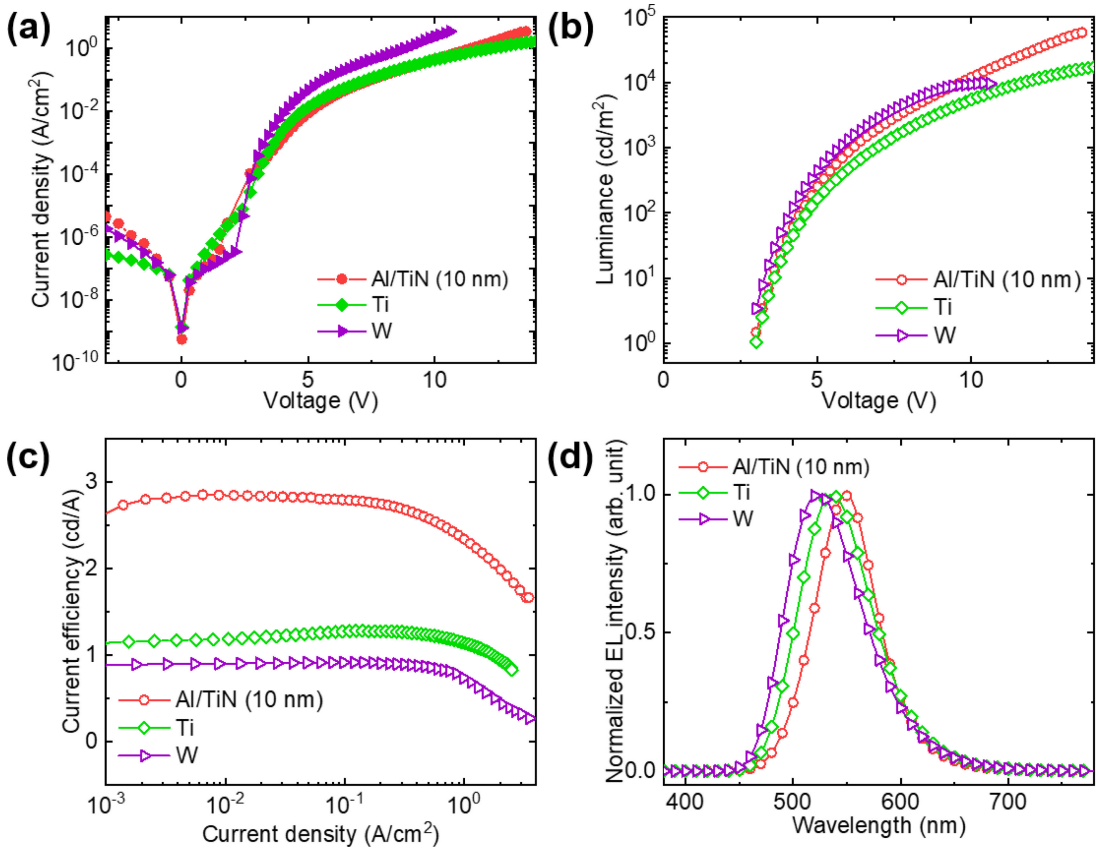

Fig. 4. (a) *J-V*, (b) *L-V*, (c) current efficiency, and (d) normalized *EL* spectra of devices with different bottom metal anodes.

same voltage. This result coincided with the result for HODs, shown in Fig. 3(a). The device with W also had higher luminance compared with the other devices, in spite of its low optical reflectance. The device with Al/TiN (10 nm) had higher luminance at the same voltage compared with the device with Ti, owing to the higher reflectance of Al/TiN (10 nm) compared with Ti, as shown in Fig. 1. For example, the devices with W, Al/TiN (10 nm), and Ti anode had, respectively, luminance values of ~1,312 cd/m^2, ~856 cd/m^2, and ~479 cd/m^2 at the same voltage of 6 V. However, the device with Al/TiN (10 nm) had a much higher maximal luminance of 57,961 cd/m^2 compared with 9,777 cd/m^2 for the device with W. This result was attributed to the electron-hole balance of the device. In the case of the device with W anode, there were many more holes than electrons in the recombination zone of the EML, because the W anode effectively injected holes from the anode to the organic layer, as shown in Fig. 3(a), and the hole mobility (on the order of 10^{-4} cm^2/V·s) of NPB was higher than the electron mobility (on the order of 10^{-5} cm^2/V·s) of Alq_3 [21], [22]. As a result, extra holes that did not form excitons quenched the emission, which decreased the device's maximal luminance in the high-voltage region. This can also be confirmed by inspecting the efficiency results in Fig. 4(c). The devices with Al/TiN, Ti, and W had current efficiency of ~2.8 cd/A, ~1.3 cd/A, and ~0.9 cd/A, respectively, at ~0.1 A/cm^2. The device with Al/TiN had higher current efficiency compared with other devices due to the higher optical reflectance of Al/TiN (10 nm) compared with Ti and W. The device with Ti had slightly higher current efficiency compared with the device with W, owing to relatively higher optical reflectance and good charge balance of Ti anode compared with W anode. In other words, low optical reflectance and charge balance of the device with the W anode reduced the current efficiency of the device in spite of its good hole injection property. Fig. 4(d) shows the

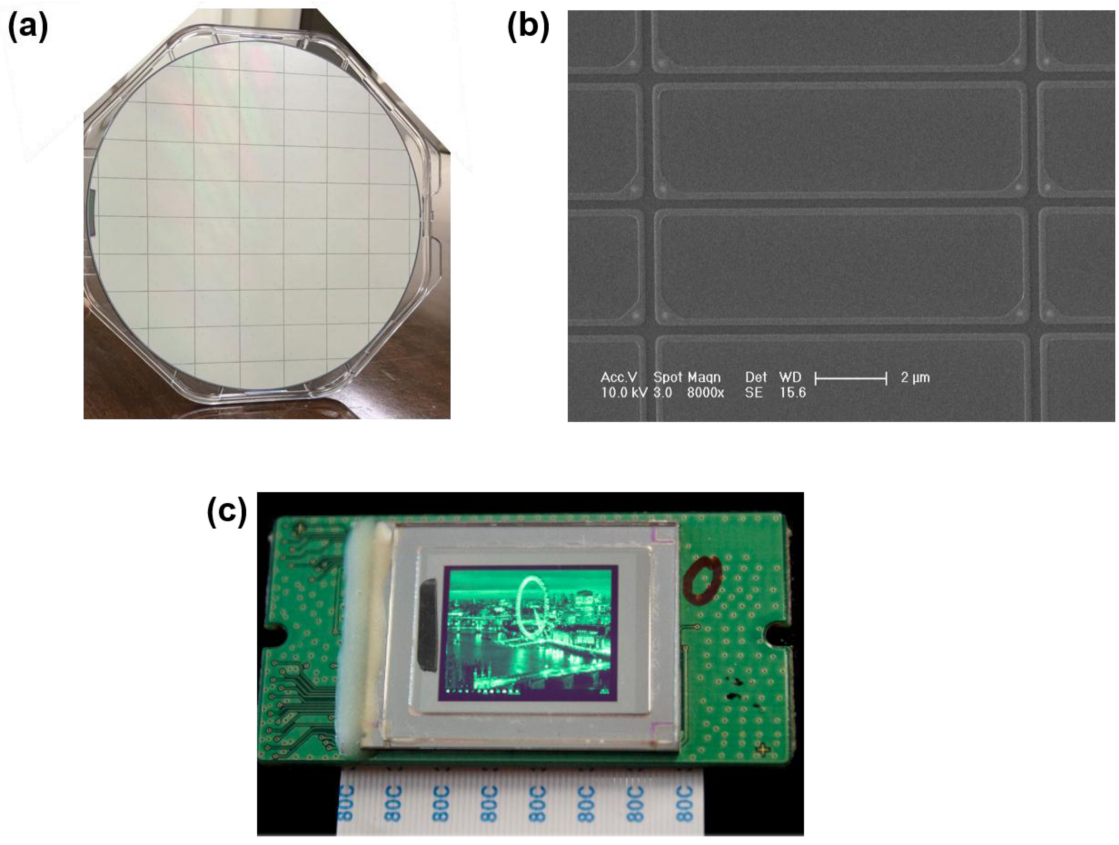

Fig. 5. (a) Photograph of the 8-inch wafer for the OLED microdisplay panel, (b) SEM image of patterned metal anode sub-pixels on the CMOS-processed backplane, and (c) operating image of the fabricated OLED microdisplay panel.

TABLE 2
Features of the OLED Microdisplay Panel With the CMOS IC

Item	Specification
Resolution	1280 × 3 × 1024
Pixel pitch	10.8 µm × 3 × 3.6 µm
Active area size	13.8 × 11.2 mm^2
Frame rate	90 Hz (max)
Power	1.2 V, 5.5 V

normalized EL spectra of the devices at ~1,000 cd/m^2, for different bottom anode metals. Each device exhibited slightly different EL emission peaks and full-width-at-half-maxima (FWHM), owing to their different micro-cavity effect. Micro-cavity effect typically consists of the Fabry-Perot factor and the two-beam interference factor [23], [24]. These two factors are determined by the micro-cavity length, the reflectance value at the electrode-organic interface, the refractive index of materials,

phase changes at the electrode-organic interface, the transmittance of semi-transparent electrode, and the location of the emission zone from the organic/reflective metal electrode interface. The device with Al/TiN (10 nm) showed main emission peak at 549 nm with FWHM of 68 nm. Since the Al/TiN (10 nm) layer had a high optical reflectance value which was high in the long wavelength region rather than the short wavelength region and the device with Al/TiN (10 nm) had a longer micro-cavity length due to TiN (10 nm) layer compared with other devices, the main emission peak of EL spectra moved to longer wavelength region and the FWHM became narrower compared with typical photoluminescence spectra of Alq_3 [25]. The devices with Ti and W exhibited main emission peaks at 537 nm and 523 nm, and 80 nm and 83 nm, respectively. Their different main emission peaks may be due to their different refractive index [26]–[28] and phase changes at the bottom anode-organic interface because their micro-cavity lengths were same and optical reflectance value difference is not large. Their similar FWHM may be owing to the similar optical reflectance spectra shape depending on wavelengths and small optical reflectance difference of the Ti and W layer. The Commission Internationale de L'Eclairage (CIE) 1931 color coordinates of the devices with Al/TiN (10 nm), Ti, and W were (0.353, 0.605), (0.325, 0.600), and (0.289, 0.584), respectively.

A green monochromatic OLED microdisplay was implemented with the 0.11 μm CMOS process. Based on the results for TEOLEDs in Fig. 4, the Al/TiN layer was selected as the anode of the OLED microdisplay panel. The sub-pixels of the OLED microdisplay panel require very weak currents to represent low gray levels such as 1 cd/m^2, owing to the display's very small size. For example, a pixel in the OLED microdisplay panel consists of three 3.6 μm $\times$ 10.8 μm sub-pixels, and the current of 6.48 $\times$ 10^{-13} A is required for 1 cd/m^2 to ensure the device's current efficiency of 60 cd/A. It is difficult to control such a small value by the driving circuit in the backplane. However, the necessary current was increased 20-fold, to 1.296 $\times$ 10^{-11} A, when the device's efficiency was 3 cd/A, allowing to easily control low gray levels. Therefore, in this work we intentionally used the device structure based on NPB/Alq_3 for OLED microdisplay panels despite its low efficiency. Of course, driving technologies such as the well-designed pixel driver [29] or the time pulse modulation method can be other solutions for expressing low gray levels of around 1 cd/m^2. Fig. 5(a) shows a photograph of the 8-inch wafer for the OLED microdisplay panel. The voltage of 1.2 V is for logic circuits while the voltage of 5.5 V is for pixel circuits. Fig. 5(b) shows a SEM image of the anode pixel patterning. The pixel density is $\sim$2,351 PPI, and the active area of the panel is 0.7 inch in diagonal. The resolution of the OLED microdisplay panel is 1,280 $\times$ 3 $\times$ 1,024, which corresponds to SXGA. Fig. 5(c) shows the operating image of the fabricated OLED microdisplay panel. Table 2 lists the main features of the fabricated OLED microdisplay panel.

4. Conclusions

We investigated the optical and surface properties of CMOS-based Al/TiN, Ti, and W metal layers. In addition, hole-injection characteristics of the different metal layers were compared by using HODs. The Al/TiN layer was found to be optically advantageous and the W layer had a good hole-injection property. The TEOLEDs with Al/TiN (10 nm) bottom anode had slightly lower current density and luminance at the same voltage, compared with those of the device with W, while they exhibited higher current efficiency and maximal luminance. Based on the TEOLEDs results, we designed and fabricated a SXGA resolution green monochromatic OLED microdisplay using CMOS IC with the Al/TiN anode. The fabricated OLED microdisplay panel was successfully operated with little defects.

References

[1] O. M. Tepper *et al.*, "Mixed reality with HoloLens: Where virtual reality meets augmented reality in the operating room," *Plastic Reconstructive Surg.*, vol. 140, no. 5, pp. 1066–1070, 2017.

[2] R. Yung and C. Khoo-Lattimore, "New realities: A systematic literature review on virtual reality and augmented reality in tourism research," *Current Issues Tourism*, doi: 10.1080/13683500.2017.1417359.

[3] V. C. Vijay, M. Lees, P. Chima, and C. Chapman, "Augmented reality environment for engineering distance leaners to acquire practical skills," in *Proc. 13th Int. Conf. Remote Eng. Virtual Instrum.*, 2016, pp. 215–223.
[4] H. Zervos, "Augmented reality and virtual reality smart eyewear: Forecasts for the next decade," in *SID Int. Symp. Dig. Tech. Pap.*, vol. 47, pp. 150–152, 2016.
[5] H. Okumura and T. Sasaki, "Hyperrealistic frameless display for future displays," *J. Inf. Display*, vol. 18, pp. 49–56, 2017.
[6] U. Yang, N.-G. Kim, and K.-H. Kim, "Augmented system for immersive 3D expansion and interaction," *ETRI J.*, vol. 38, no. 1, pp. 149–158, 2016.
[7] P. E. Malinowski *et al.*, "High resolution photolithography for direct view AMOLED AR displays," in *SID Int. Symp. Dig. Tech. Pap.*, vol. 49, pp. 999–1002, 2018.
[8] A. Ghosh *et al.*, "Ultra-high-brightness 2K x 2K full-color OLED microdisplay using direct patterning of OLED emitters," in *SID Int. Symp. Dig. Tech. Pap.*, vol. 48, pp. 226–229, 2017.
[9] M. J. Park, S. K. Kim, R. Pode, and J. H. Kwon, "Low absorption semi-transparent cathode for micro-cavity top-emitting organic light emitting diodes," *Organic Electron.*, vol. 52, pp. 153–158, 2018.
[10] V. Adamovich, A. Shoustikov, and M. E. Thompson, "TiN as an anode material for organic light-emitting diodes," *Adv. Mater.*, vol. 11, no. 9, pp. 727–730, 1999.
[11] Y. Ji, F. Ran, H. Xu, W. Shen, and J. Zhang, "Improved performance and low cost OLED microdisplay with titanium nitride anode," *Organic Electron.*, vol. 15, pp. 3137–3143, 2014.
[12] C. Y. Park, C.-H. Hyun, S. K. Kang, B.-C. Kwak, and O.-K. Kwon, "XGA OLED microdisplay for personal display application," in *Proc. Int. Display Workshops*, 2011, vol. 18, pp. 815–818.
[13] D. L. Rode, V. R. Gaddam, and J. H. Yi, "Subnanometer surface roughness of dc magnetron sputtered Al films," *J. Appl. Phys.*, vol. 102, 2007, Art. no. 024303.
[14] Y. L. Jeyachandran *et al.*, "Properties of titanium thin films deposited by dc magnetron sputtering," *Mater. Sci. Eng. A*, vol. 431, pp. 277–284, 2006.
[15] H. B. Michaelson, "The work function of the elements and its periodicity," *J. Appl. Phys.*, vol. 48, pp. 4729–4733, 1977.
[16] L. P. B. Lima, J. A. Diniz, I. Doi, and J. G. Fo, "Titanium nitride as electrode for MOS technology and Schottky diode: Alternative extraction method of titanium nitride work function," *Microelectron. Eng.*, vol. 92, pp. 86–90, 2012.
[17] J. Chang *et al.*, "Asymmetric supercapacitors based on graphene/MnO_2 nanospheres and graphene/MoO_3 nanosheets with high energy density," *Adv. Functional Mater.*, vol. 23, pp. 5074–5083, 2013.
[18] Y. H. Kim, S. Kwon, J. H. Lee, S. M. Park, Y. M. Lee, and J. W. Kim, "Hole injection enhancement by a WO_3 interlayer in inverted organic light-emitting diodes and their interfacial electronic structures," *J. Phys. Chem. C*, vol. 115, pp. 6599–6604, 2011.
[19] X. Yang *et al.*, "Solution processed tungsten oxide interfacial layer for efficient hole-injection in quantum dot light-emitting diodes," *Small*, vol. 10, no. 2, pp. 247–252, 2014.
[20] J. F. Moulder, W. F. Stickle, W. F. Stickle, P. E. Sobol, and K. D. Bomben, *Handbook of X-Ray Photoelectron Spectroscopy.* Eden Prairie, MN, USA: Perkin-Elmer Corporation, 1992.
[21] Z. Deng, S. T. Lee, D. P. Webb, Y. C. Chan, and W. A. Gambling, "Carrier transport in thin films of organic electroluminescent materials," *Synthetic Met.*, vol. 107, pp. 107–109, 1999.
[22] S. Barth *et al.*, "Electron mobility in tris(8-hydroxy-quinoline)aluminum thin films determined via transient electroluminescence from single- and multilayer organic light-emitting diodes," *J. Appl. Phys.*, vol. 89, no. 7, pp. 3711–3719, 2001.
[23] H. Cho, C. Yun, and S. Yoo, "Multilayer transparent electrode for organic light-emitting diodes: tuning its optical characteristics," *Opt. Exp.*, vol. 18, no. 4, pp. 3404–3414, 2010.
[24] H. Lee, J. Lee, J.-I. Lee, and N. S. Cho, "Improvement of colour gamut in bottom-emission organic light-emitting diodes using micro-cavity structure embedded cathodes," *Electronics*, vol. 7, no. 9, pp. 155(1)–155(9).
[25] A. B. Djurišic, T. W. Lau, L. S. M. Lam, and W. K. Chan, "Influence of atmospheric exposure of tris(8-hydroxyquinoline) aluminum (Alq_3): A photoluminescence and absorption study," *Appl. Phys. A, Mater. Sci. Process.*, vol. 78, pp. 375–380, 2004.
[26] D. W. Lynch, C. G. Olson, and J. H. Weaver, "Optical properties of Ti, Zr, and Hf from 0.15 to 30 eV," *Phys. Rev. B*, vol. 11, no. 10, pp. 3617–3624, 1975.
[27] J. H. Weaver, C. G. Olson, and D. W. Lynch, "Optical properties of crystalline tungsten," *Phys. Rev. B*, vol. 12, no. 4, pp. 1293–1297, 1975.
[28] B. L. Henke, P. Lee, T. J. Tanaka, R. L. Shimabukuro, and B. K. Fujikawa, "Low-energy x-ray interaction coefficients: Photoabsorption, scattering, and reflection: $E = 100$–2000 eV $Z = 1$–94," *At. Data Nucl. Data Tables*, vol. 27, no. 1, pp. 1–144, 1982.
[29] T. Fujii *et al.*, "4032 PPI high-resolution OLED microdisplay," *J. Soc. Inf. Display*, vol. 26, no. 3, pp. 178–186, 2018.